# Muon event localisation with AI

Heredge, J.; Archer, J. W.; Duffy, A. R.; Brown, J. M.C.; Guatelli, S.; Scutti, F.; Krishnan, S.; Webster, C.

**Citation (APA)**
Heredge, J., Archer, J. W., Duffy, A. R., Brown, J. M. C., Guatelli, S., Scutti, F., Krishnan, S., & Webster, C. (2021). Muon event localisation with AI. *Nuclear Instruments and Methods in Physics Research, Section A: Accelerators, Spectrometers, Detectors and Associated Equipment*, *1001*, Article 165237. https://doi.org/10.1016/j.nima.2021.165237

**Important note**
To cite this publication, please use the final published version (if applicable).
Please check the document version above.

# Muon event localisation with AI

J. Heredge [a], J.W. Archer [b], A.R. Duffy [a,*], J.M.C. Brown [c,b], S. Guatelli [b], F. Scutti [d], S. Krishnan [e], C. Webster [e]

[a] Centre for Astrophysics and Supercomputing, Swinburne University of Technology, PO Box 218, Hawthorn, VIC 3122, Australia
[b] Centre for Medical Radiation Physics, University of Wollongong, Wollongong, Australia
[c] Department of Radiation Science and Technology, Delft University of Technology, The Netherlands
[d] The University of Melbourne, Parkville, VIC 3010, Australia
[e] Swinburne University of Technology, John Street, Hawthorn, VIC, Australia

## ARTICLE INFO

## ABSTRACT

Low-cost muon detectors utilising cheap plastic scintillators and a limited number of individual silicon photomultipliers (SiPMs) offer a compelling approach to cheap experimental designs, provided the event localisation of a traversing particle can be accurately determined. In this theoretical work, we use Geant4 to simulate a diverse range of detector configurations, shapes and SiPM photosensors, predicting the light intensity received at a given SiPM. Testing a range of methods to localise muon events we determine that machine learning techniques outperform analytic models, and of these, a simple gradient boosted framework is the most reliably accurate localisation technique for our simulated scintillators. We find that a simple square scintillator outperforms other geometries and that AI performs, when applied to this shape, with a linear relationship between the positional accuracy of the event recovery and the average distance between photosensors around the detector perimeter.

## 1. Introduction

For small-scale particle detection experiments it may often be impractical to use sophisticated and expensive technologies, such as drift chambers [1] or charge-coupled devices (CCDs) [2], in order to locate the position of a particle event (although see CREDO [3] as a large scale example of using smartphone CCDs for muon detection). One cost-effective method of particle location is to rely on cheap, plastic scintillators [4,5] and low-cost silicon photomultipliers (SiPMs) photosensors [6,7]. To go beyond event counting to event reconstruction, we require knowledge of where the muon traversed the detector. It is, in theory, possible to measure the intensity of light in several SiPM photosensors positioned around the scintillator as the particle passes through this scintillator, and triangulate the location of the signal. While seemingly a well-posed problem, due to reflections within the material, a simple analytic triangulation algorithm in which the intensity $I \propto \frac{1}{r^2}$, where $r$ is the distance, may not perform well as we will show in this work.

The task of this paper is to determine if it is possible to use low numbers of SiPMs to reconstruct the muon location when traversing a scintillator for the purpose of delivering a low-cost detector in reality. We will determine if the $I \propto \frac{1}{r^2}$ technique is feasible and identify a superior alternative to it if not. In particular, we will explore more complex analytic models as well as several machine learning (ML)

techniques and analyse their respective performances. At its most fundamental, this work is a reconstruction challenge in which a muon event traverses through the plastic scintillator at position $\vec{x} = (x, y)$ whereby optical photons are emitted. The intensity of the optical photons are measured by $N$ photomultipliers optically coupled to the scintillator. These $N$ intensity measurements form an $N$ dimensional vector for the event denoted by $\vec{I}$. The aim is to produce a model $\mathcal{M} : \mathbb{R}^N \to \mathbb{R}^2$ that takes intensities $\vec{I}$ as an input and outputs the position $\vec{x} = \mathcal{M}(\vec{I})$. In addition, we will further extend the analysis of these techniques by investigating a range of scintillation geometries and photomultiplier locations (and numbers) to demonstrate the trade-off between lowering component cost and event reconstruction accuracy to inform future instrumentation and experimental design choices.

While our motivation is to deduce particle location in a detector, the formulation is general and may be applied to other problem domains. For example, a common application is indoor positioning systems to attempt the locate the position of an electronic device using the received signal strength of various WiFi detectors within a building [e.g. 8].

To provide the data for our idealised muon reconstruction work we generate an extensive suite of test data using Geant4 [9–11], as explained in Section 2. In particular, Geant4 simulations for a range of detector configurations as outlined in Section 3 are used to train the ML-algorithms and to evaluate the accuracy of the ML-based results

obtained in this work. We initially attempt to reconstruct the location of the muon events using an analytic formalism in Section 4 and then move to more complex AI techniques in Section 5. We explore a range of detector configurations including scintillator geometries (comparing fiducial square to circle, and then a range of polygons), number of photosensors (i.e. sample points) and their spacing in Section 6. We discuss these results and implications for future work in Section 7 before concluding in Section 8 on what the optimal configuration for a low-cost detectors may be.

## 2. Geant4 simulations

There are a large range of experimental configurations possible when considering a plastic scintillator for use in low-cost experiments. To offer the broadest insights to the instrumental design of these future experiments we adopt the most general assumptions that can be modelled. A simple, uniform, plastic scintillator with no internal defects; high reflective paint-coating and idealised photosensors locations.

We used Monte Carlo simulations, based on the LXe extended example in Geant4 10.05.p01 [9–11], to calculate the theoretical response of the proposed detector for 3 GeV muons incident normally on the detector surface. Again, this is a highly idealised experiment as muons occur with a large angular distribution [e.g.12] but the majority of muons will occur close to zenith; an assumption that is increasingly accurate the deeper underground an experiment is located for example.

Geant4 *FTFP_BERT* physics list was adopted in this work as it is the default in the LXe example. The *G4EmStandardPhysics* constructor was substituted with *G4EmStandardPhysics_option4*, which is deemed to be the most accurate e.m. physics constructor in Geant4 for EM physics processes [13]. Default step length and low energy particle cutoff limits of this physics constructor were implemented as they have been shown to reliably produce a wide variety of experimental results [13,14]. The emission of fluorescence radiation was enabled. The threshold of production of secondary particles was set equal to 0.7 mm, which is less than one tenth the thickness of the scintillator slab. Optical photon processes, scintillation and Cherenkov radiation production were modelled as well.

We found that approximately $8 \times 10^5$ simulated incident muons per detector design provided results with adequate statistics. The output of the simulation is the photon count at the windows of the SiPMs and the incident position of the muon for each incident particle. The detection efficiency of the SiPMs are then convolved with the photon counts resulting from the simulations to provide a final intensity value that the ML-based detection algorithms can utilise.

### 2.1. Scintillator properties

In this idealised model, the scintillator bulk properties were based on the EJ-208 specification sheet [15] as summarised in Table 1.

In the simulation, the scintillator was modelled in vacuum and coated with 0.11 mm thick EJ-205 $TiO_2$ paint, a standard low-cost coating to ensure significant internal reflections and boost received signals at the photosensor locations. In Fig. 1(a) we show the assumed reflectivity of optical photons at the interface between the scintillator and the $TiO_2$ paint that covers it. While experiments may explore different coating combinations, the flat (and high) reflectivity across the visible spectrum provides a compelling yet simple baseline design. Others of course, may choose to vary this if there was a particular wavelength they wanted to optimise the design for.

Fig. 1(b) shows the spectrum of the optical photons emitted by polyvinyl toluene (PVT), this data is derived from the EJ-208 specification sheet [15]. Quenching effects are modelled using Birk's Law, with a Birk's Constant of $0.128 \, mm \, eV^{-1}$, derived from the experimentally determined value of the BC-104 PVT scintillator [16].

Optical photons are counted when they traverse the SiPM windows with the resulting intensity recorded after convolving these counts with the quantum efficiency of the SiPMs outlined in Fig. 1(c).

**Table 1**
Photon energy independent bulk properties of the simulated scintillator [15].

| Properties | |
|---|---|
| Scintillation Yield | $9200 \, mm^{-1}$ |
| Refractive Index | 1.58 |
| Density | $1.023 \, g \, cm^{-3}$ |
| Absorption Length | 400 cm |
| Decay Time | 3.3 ns |
| Birk's Constant | $0.128 \, mm \, MeV^{-1}$ |

The SiPMs windows have a total area of $7 \times 7 \, mm^2$ and a $6 \times 6 \, mm^2$ sensitive area. The small remaining area is simulated to be aluminium. Each SiPM window is represented in red for the square and circular shaped configurations in Figs. 2(a) and 2(b), respectively. We have also explored other geometries beyond these fiducial cases, to characterise and identify the optimal set-up for the event reconstruction of incident muons. These are outlined in the following section.

### 2.2. Detector configurations

Various configurations of the detector were simulated to study the ability of ML-techniques to reconstruct the position of the muon position when traversing the scintillator (see figure Fig. 2). The thickness of the detector in the direction of the muons' incidence is kept constant and equal to 10 mm. The shape of the side at right angles with the incident muons is instead changed (plane, circle and polygon). In Fig. 2(a) we see the detector with planar, i.e. square, sides and in Fig. 2(b) we show the positioning of the SiPMs along circular sides. Again, the muons are normally incident on the device as shown in Fig. 2.

For the square scintillator, edge widths of 100 mm, 150 mm and 200 mm were used with 4, 6 and 8 SiPMs mounted on the edges respectively. The 4 SiPM configuration consists of a single SiPM mounted on each thin edge, the position of which is determined by an offset value from the left edge. This offset value varies as described below and shown in Fig. 3. The 6 SiPM configuration introduces two extra SiPMs on two opposing sides, which are governed by a second offset value. The 8 SiPM configuration consists of 2 SiPMs on each edge.

For the circular scintillator, the areas of the circle used corresponded to a whole, one half and one quarter of the surface area of the $200 \times 200 \, mm^2$ square scintillator. Each area was simulated with 3, 4, 5, 6, 7 and 8 SiPMs, evenly distributed around the thin edge of the circular scintillator. Again, the square and circular detector geometries can be seen in Figs. 2(a) and 2(b) respectively.

For the polygon scintillator, a polygon is generated with an equivalent surface area to that of the $200 \times 200 \, mm^2$ square scintillator. A SiPM is mounted on each edge, giving a polygon with $N$ sides and $N$ total SiPMs. The SiPMs are mounted in three configurations: at the middle of the edge, a quarter of the way along the edge and directly on the edge corner (in practice the SiPM is effectively offset 3.5 mm from the corner to affix it entirely on the face of the scintillator, but for convenience this will be stated henceforth as the edge corner). We show this configuration pattern for a pentagon shape in Fig. 3.

Each configuration is simulated using a perpendicularly incident $\mu^+$ field with an energy of 3 GeV. For every muon which traverses the detector geometry, the incident position $(x, y)$ on the face of the detector is recorded as well as the number of optical photons detected at each SiPM.

## 3. Light-yield results

Fig. 4 shows the number of optical photons traversing any of the SiPM windows, produced by a muon incident on the scintillator in position $(x, y)$. Using 4 SiPMs on the square scintillator, regions of low

(a) Reflectivity of TiO₂ paint covering scintillator [17].



(b) Scintillator emission optical photon spectrum [15].



(c) Detection efficiency of the SiPMs [18].
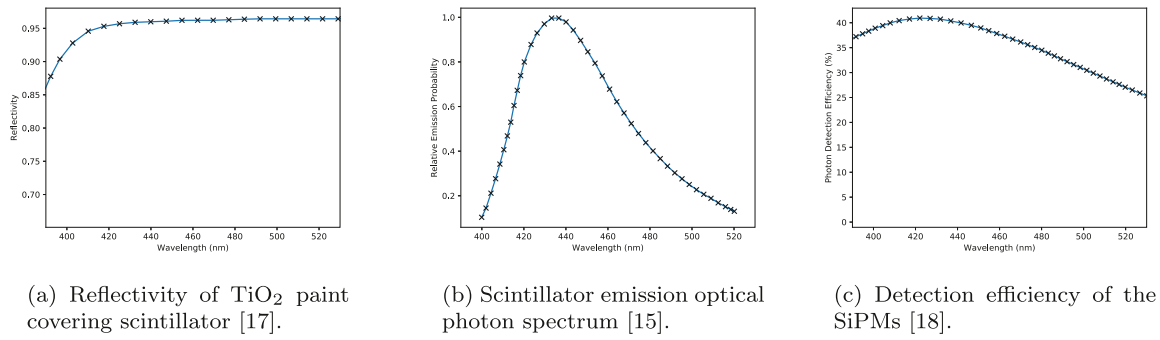
**Fig. 1.** Photon wavelength dependent scintillator parameters modelled in this work (see Refs. [17,15,18]).



(a) Square-based scintillator with SiPMs on each edge. A sample muon trajectory is shown with the incident position recorded. The scintillating slab is contained within the painted volume.



(b) Cylindrical scintillator with SiPMs distributed evenly around the circumference.
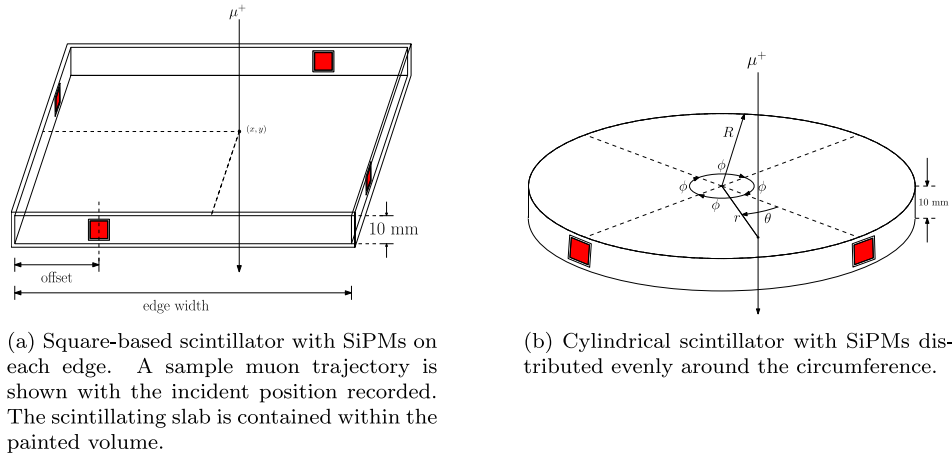
**Fig. 2.** The square and circular scintillator geometries simulated. The windows of the SiPMs are shown in red. (For interpretation of the references to colour in this figure legend, the reader is referred to the web version of this article.)



(a) SiPMs mounted in the middle of the edge.



(b) SiPMs mounted a quarter along the edge.



(c) SiPMs mounted on the edge.
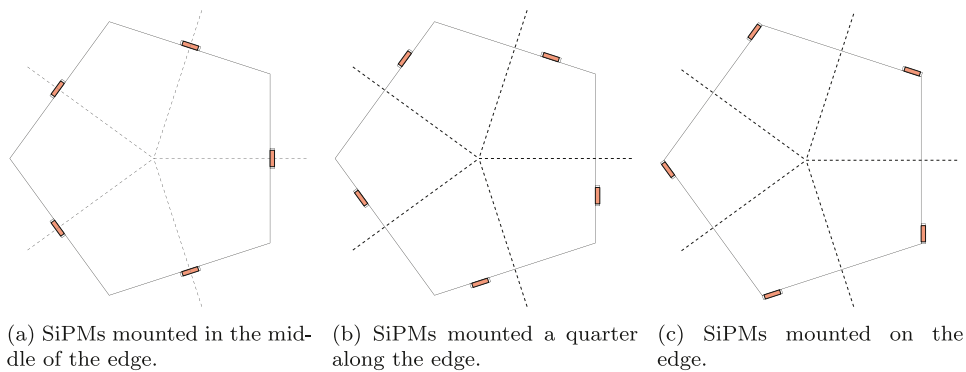
**Fig. 3.** SiPM configurations used for the polygon scintillator. Here, a pentagon is used as an example.

response arise, clearly visible as dark blue in Fig. 4(a). While increasing the number of SiPMs reduce these areas, they are still prevalent with 6 and 8 SiPMs as seen in Fig. 4(b) and Fig. 4(c) respectively. The asymmetry in the response of the SiPM photosensor, as given by yellow pixels of higher photon count detection in Fig. 4 in the clockwise direction, indicates the face of the window that the SiPM is affixed too. As shown in Fig. 2(a), the SiPM at a corner edge is in reality still on one side, rather than a sheared corner. The offset from that corner is small, just 3.5 mm, however it will preferentially collecting more rebounding light normal to that face.

No such asymmetry is seen in the circular geometry of Fig. 5 as the SiPMs are affixed to the circular exterior. The improvement in the light collection of increasing SiPM photosensors as seen for the square geometry is, however, reflected in the circular shaped scintillators.

The results show that in these geometries, the detector response has a strong dependence on the position of the traversing muon. We would like to reduce the regions of low response to improve the efficiency of muon detection, as these could be problematic from the perspective of creating a viable low-cost plastic scintillator detector with a low number of SiPMs.

To solve this problem, different geometrical configurations of the detector system were studied. The left column of figure Fig. 6 shows the results for the square scintillator where the regions of low response can be seen to simply rotate around. These regions tend to be on the borders of the scintillator, between the SiPMs and at the centre. The signal is also lower at the corners due to the effects of internal reflection.

Indeed, this behaviour can be generalised for the other polygon shapes explored in Fig. 6, allowing one to anticipate and select a design to optimise the response of the detector. Mounting the SiPMs
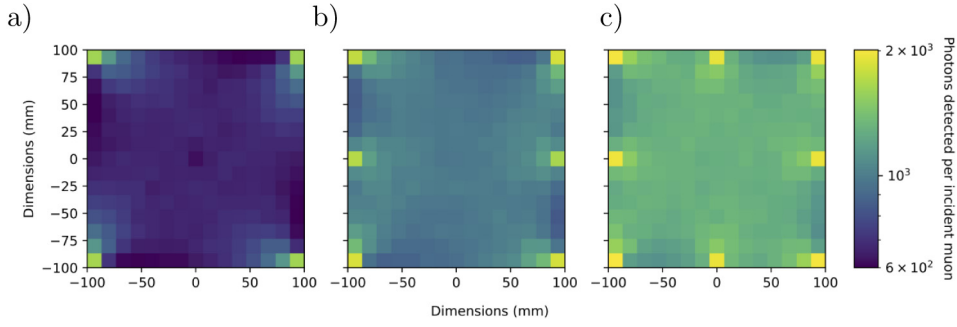
**Fig. 4.** Detector response with 4, 6 and 8 SiPMs shown by subfigures (a), (b) and (c) respectively, on the edges of the square scintillator.
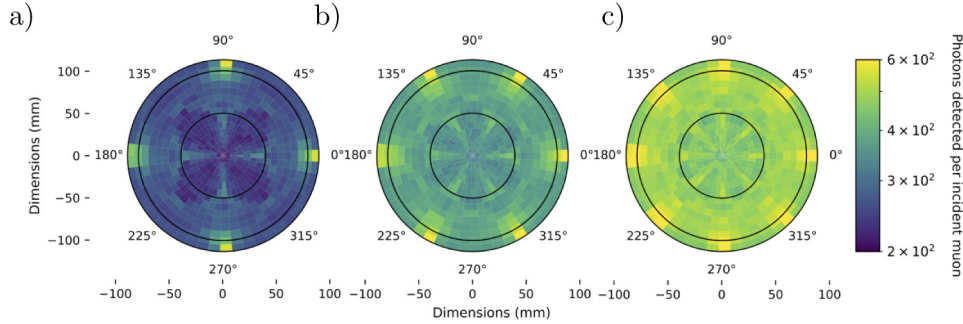


**Fig. 5.** Detector response with 4, 6 and 8 SiPMs shown by subfigures (a), (b) and (c) respectively, on the edges of the cylindrical scintillator.

in the middle of the polygon edges gives large regions of small received photon counts as seen in Fig. 6(a). The area of higher counts approximately forms a smaller rotated polygon with the vertices being at each SiPM. The SiPMs mounted a quarter along the edge resolve these regions much better as in Fig. 6(b), and the edge mounted SiPMs seen in Fig. 6(c) are better again, similar to the lower count regions as shown with the square scintillator. As we explore in Fig. 7 below, this visual trend of configurations belies the real quantitative difference. Although we note in general the differences in the configurations for *received* photon counts is minor, the performance later on for event reconstruction is not.

In Fig. 7 we see the quantitative impact of the different configurations explored in Fig. 6 with a SiPM along each edge of a polygon. Although more SiPMs will result in more photons being detected as expected, Fig. 7(a) shows that there is a diminishing return with increasing SiPMs detecting fewer photons *per* SiPM. We also see the placement of SiPMs on the quarter edge to also perform more poorly for the square and pentagon shapes.

In Fig. 7(b) we defined the global detector efficiency (GDE) estimated by the total number of photons detected, divided by the number of photons produced by all generated muons. This GDE was then normalised by the maximum GDE, in this case the octagon polygon, to make the relative GDE. It is clear that increasing the number of SiPMs will result in a higher number of detected photons. Visually this can be seen by the increasingly green colour in Fig. 6 from (i) to (iii) as the SiPM count increased.

Perhaps most importantly for event reconstruction, was the uniformity of photon count detection, as calculated using the standard deviation across the scintillator, divided by the number of SiPMs in Fig. 7(c). This is the quantitative estimate of the range of colours seen by eye in Fig. 6, and a lower number indicates reduced dead zones across the detector. Essentially, all configurations benefit from increasing the number of SiPMs (visually this is the diminishing of the dark regions) although the corner mounted detectors are marginally worse than the mid or quarter placed SiPMs.

Using this wide range of simulated photon outputs for muons incident on a range of geometries, number of SiPM photosensors as well

as their positions/separation lengths we can now explore the optimal configuration under which these event locations can be recovered.

## 4. Analytical reconstruction

We remind the reader that the entry of each simulated muon using Geant4 represents a known 'true' event position along the scintillator surface, and the resulting photon count at each SiPM photosensor that results is recorded. These intensity measurements form the elements of an intensity vector $\vec{I}$ for that event.

The process of localising an event on the detector surface $\vec{x} = (x, y)$ from the light intensities $\vec{I}$ measured by $N$ photosensors requires determining a model $\mathcal{M} : \mathbb{R}^N \to \mathbb{R}^2$ that results in $\vec{x} = \mathcal{M}(\vec{I})$. Before exploring more complex machine learning models we first explore analytical approaches. In particular, two reconstruction methods were investigated as outlined in the next two subsections.

### 4.1. Weighted average reconstruction

In order to compare the reconstruction performance of machine learning methods, a standard reconstruction technique based on a weighted average is first presented in this section. This is similar to the method outlined in [7] and [19]. The reconstructed position is determined by computing a weighted average of the intensity readings from each SiPM using

$$\vec{x}_{\text{reco}} = \frac{\sum_k I_k^2 \, \vec{x}_k}{\sum_k I_k^2}, \tag{1}$$

where $\vec{x}_k$ represents the position of SiPM $k$ in the two-dimensional (x,y) plane, and $I_k$ its intensity measurement. The results are illustrated in Fig. 8, where the reconstructed positions are shown together with the true position, i.e. where muons are sourced with Geant4, cumulatively for all events. This figure also includes different geometries of a square in (i), pentagon in (ii) and octagon in (iii), as well as various photosensor positions along the edge of the scintillator as will be introduced in the following sections (in the centre or middle of an edge in Fig. 8(a) and a quarter from the edge in Fig. 8(b)). For now it is sufficient to note
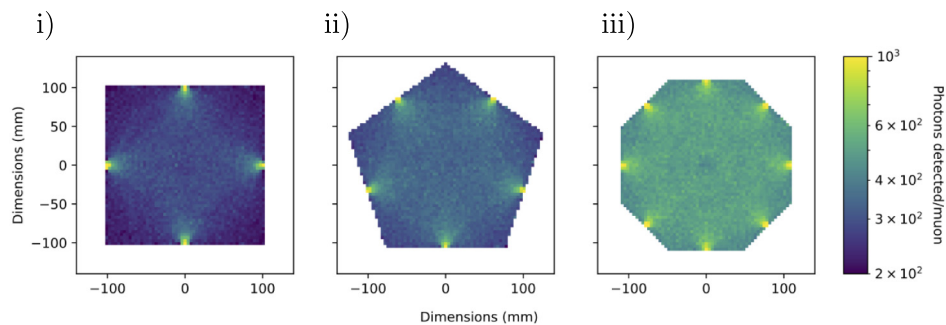
(a) Detector response for SiPMs mounted centrally, i.e. the middle, of the edges of a 4, 5 and 8 sided polygon scintillator.
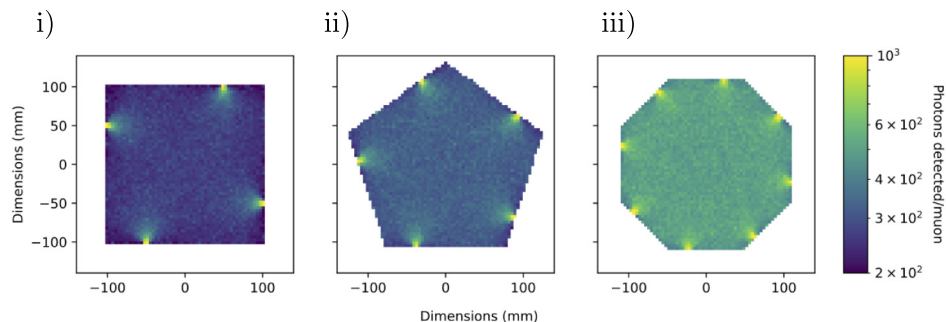


(b) Detector response for SiPMs mounted a quarter along the edges of a 4, 5 and 8 sided polygon scintillator.
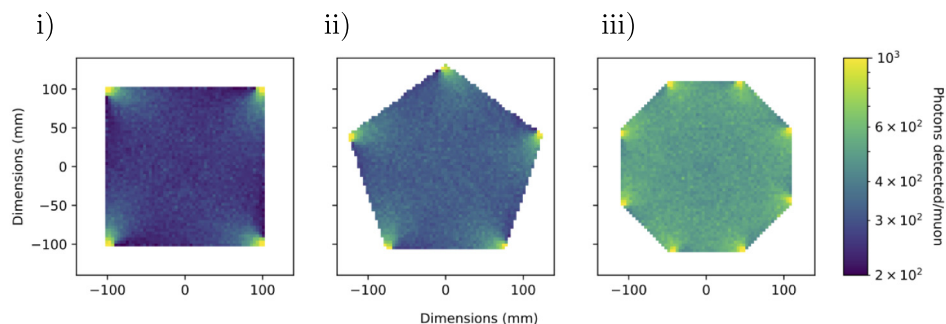


(c) Detector response for SiPMs mounted in the corners of each edge of a 4, 5 and 8 sided polygon scintillator.

**Fig. 6.** Exploring the dependence of the detector response and 'dead zones' of relatively lower photon capture through the systematic rotation of the SiPM photosensor location.

that the analytical method shows a clear bias toward reconstructing the position in the centre of the detector, with the exception of cases where the true position is close to the photosensor.

To better illustrate this, reconstructed positions for the square geometry are illustrated in Fig. 9 with red marks, where they are compared to specific clusters of true positions as the blue dots. In this square geometry configuration, the SiPMs are located in the middle of the detector sides (configuration as given by Fig. 4(a)).

The reconstruction performance of the analytical approach for scintillator area of $200 \times 200 \, \text{mm}^2$ is reported in Table 2, and is quantified by the average distance between the reconstructed and true positions for cases where the photosensor is in the middle of the detector side and cases where it is at a quarter of its edge width. For the case of the square, the offset for a SiPM from a corner is thus $100 \, \text{mm}$ for the former and $25 \, \text{mm}$ for the latter as shown visually in Fig. 6(a) and Fig. 6(b) respectively. This table can be compared with Table 7 which considers the ML-based reconstruction approach, clearly showing the ML advantage over analytical reconstruction.

**Table 2**

Average distance in [mm] between the predicted and actual position in a configuration where one SiPM is located on each side of a particular shape of the detector. All configurations have total area of $200 \times 200 \, \text{mm}^2$. Photosensors were positioned either a quarter along an edge or in the middle of an edge for the middle and last columns respectively. Middle positions are indicated by Fig. 3(a) (light yield from Fig. 6(a)) and Quarter positions in Fig. 3(b) (light yield from Fig. 6(b)).

| Number of edges | Quarter [mm] | Middle [mm] |
|---|---|---|
| 4 | 63.57 | 68.74 |
| 5 | 65.32 | 67.0 |
| 6 | 62.73 | 63.96 |
| 7 | 61.93 | 63.87 |
| 8 | 61.86 | 63.94 |

### 4.2. Analytical fit

We explore another approach that involves an analytical method, based on using the inverse square law of light propagation inside the
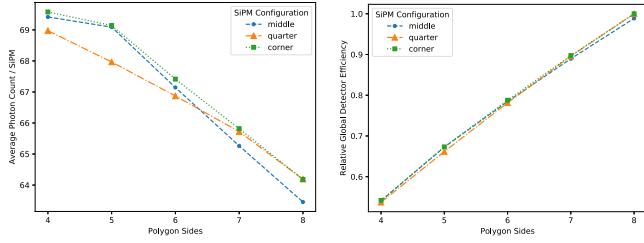
(a) Average photon count detected by a SiPM, normalised by the number of SiPMs, for each detector

(b) Global detector efficiency is the number of photons detected, divided by the number of photons produced by all generated muons
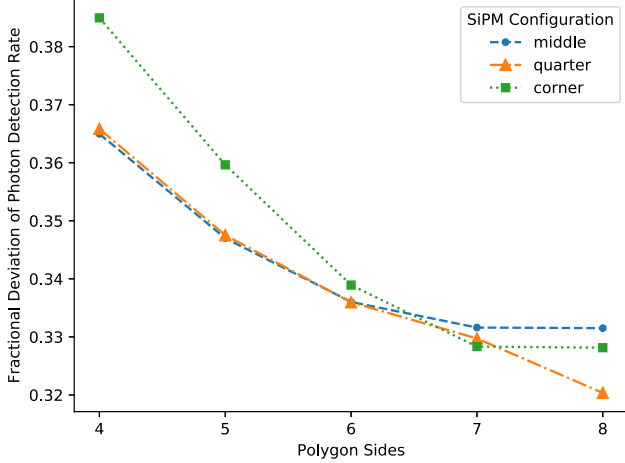


(c) Standard deviation of photons detected across the scintillator, divided by the average photon count

**Fig. 7.** Summary statistics of the detected photon counts as a function of polygon sides, in which each side has a SiPM, with different SiPM configurations (lines/points given in legend) as given in Fig. 6.

scintillator. The reconstructed position is determined by fitting the intensity readings of the SiPM photosensors according to the following function [20]

$$I(\vec{x}) \approx I_0 \alpha \frac{e^{-\alpha|\vec{x}-\vec{x}_0|}}{(\vec{x}-\vec{x}_0)^2} + \tau, \tag{2}$$

representing the intensity of the light illuminating an individual SiPM photosensor and proportional to the SiPM reading. In Eq. (2) we describe the light propagation within the scintillator according to a modified version of the standard inverse square law. This modification is to account for light reflection, attenuation through the plastic scintillator, and photosensor noise. In this formula, $I_0$ represents the original intensity of the light source, $\alpha$ accounts for the absorption of light in the scintillator, and $\tau$ represents a parameterisation of the background light caused by scattered scintillation photons. The distance between the position of the source, $\vec{x}$, and the position of the photosensor, $\vec{x}_0$, is considered to be in the two-dimensional plane (x,y) only, as no sensitivity would be provided to the reconstruction of the vertical position of the source.

The fit is performed using the *curve_fit* routine of the scipy package [21], implementing a non-linear least square minimisation procedure. A calibration procedure is described below, detailing the measurement of fit constants using simulated data.

The number of free parameters illustrated in Eq. (2) is often comparable with the number of intensity readings provided by the SiPM photosensors around the scintillator perimeter for individual events. In order to guarantee a stable fit procedure, and noticing that $I_0$, $\alpha$, and $\tau$ should not significantly vary on an event-by-event basis, a calibration procedure has been conducted where multiple events are fitted simultaneously in order to determine these parameters.

**Table 3**
Division of event regions used for the calibration procedure on a square geometry, where $B$[mm] is set as $[25, 37.5, 50]$ for edge widths in mm of $[100, 150, 200]$ respectively.

| Dataset region | $x$ | | $y$ |
|---|---|---|---|
| centre | $\in (-B, B]$ | & | $\in (-B, B]$ |
| sides | $\in (-B, B]$ | & | $\notin (-B, B]$ |
| | $\notin (-B, B]$ | & | $\in (-B, B]$ |
| corners | $\notin (-B, B]$ | & | $\notin (-B, B]$ |

In order to take into account a possible dependency of these quantities on the true position of the incident radiation across the area of the scintillator, the dataset is divided in different regions summarised in Table 3 for a square geometry. For each dataset defined in this way, all events are fitted simultaneously where the position of the light source is fixed based on the input value from the simulation. Parameters determined in this way are then set as the initial values of the fit.

Even after the calibration is performed however, the fit is affected by convergence issues, to the point that unreliable results affect most of the reconstructed points. To further improve upon the performance of the fit, the *lrm* and *dogbox* options are selected in turn when calling the *curve_fit* routine. In addition to this, fit parameters have been restricted in turn. A constraint on $\tau$ to be $\approx 0.001$ ‰ of $I_0$ has been introduced as well as trying several interval ranges for $\alpha$, either fixed to its nominal value of $\approx 2.5\mathrm{e}{-4}$ mm$^{-1}$ [15], or considering variation ranges of 1%, 5%, 10% and 30% around this value. Finally, for each of these options the fit is repeated with and without initialising the reconstructed position to the coordinates determined by the weighted average method.

The best results are obtained for the *dogbox* option while having $\alpha = 2.5\mathrm{e}{-4}$ mm$^{-1}$ and initialising the reconstructed position at the origin. An example of the fits obtained in this way is reported in Fig. 10. As evident from the plots, even under these restricted and improved conditions the overall reconstruction performance of the fitting method is worse than the weighted average one. Fitting issues are likely to arise from the formula of light propagation used, where no analytical way of modelling reflections was incorporated. We note that there are thorough investigations about this modelling present in the literature (e.g. [22]). However, as the scope of this present work is to present a general approach valid for different detector geometries, primarily by leveraging recent advances in machine learning, any additional studies to adjust the fit convergence are not pursued further.

## 5. Machine learning models

The failure to accurately recover muon event locations with analytic fits in Section 4 suggest that internal reflections and other non-linear features of the experiment are complicating the modelling effort. We therefore turn to machine learning models as ways to capture any inherent signals in the SiPM intensities beyond that which the analytic fit was able to utilise. In this Section we explore three standard machine learning models and compare their performances, with a summary of the theory and motivation of each model given.

The simulated muon events were split into three datasets: training, validation and testing. The weights for a given machine learning method are learnt using the training set. This training process is repeated with different hyperparameters (such as network depth for the Multilayer Perceptron Neural Network or the $\sigma$ value for the Probabilistic Neural Network) and its performance measured on the validation set. The hyperparameters are then set using the results of the validation set. Finally, our results show the outcome of each model when using the testing dataset, which was not previously seen by the model at any point during the training. The exact sample size of each subset may differ for a given machine learning technique employed (but is

(a) Detector response for SiPMs mounted centrally, i.e. the middle, of the edges for 4, 5, and 8 sided polygon scintillator in i), ii) and iii) panels respectively.



(b) Detector response for SiPMs mounted a quarter of its edge width for the 4, 5, and 8 sided polygon scintillator in i), ii) and iii) panels respectively.
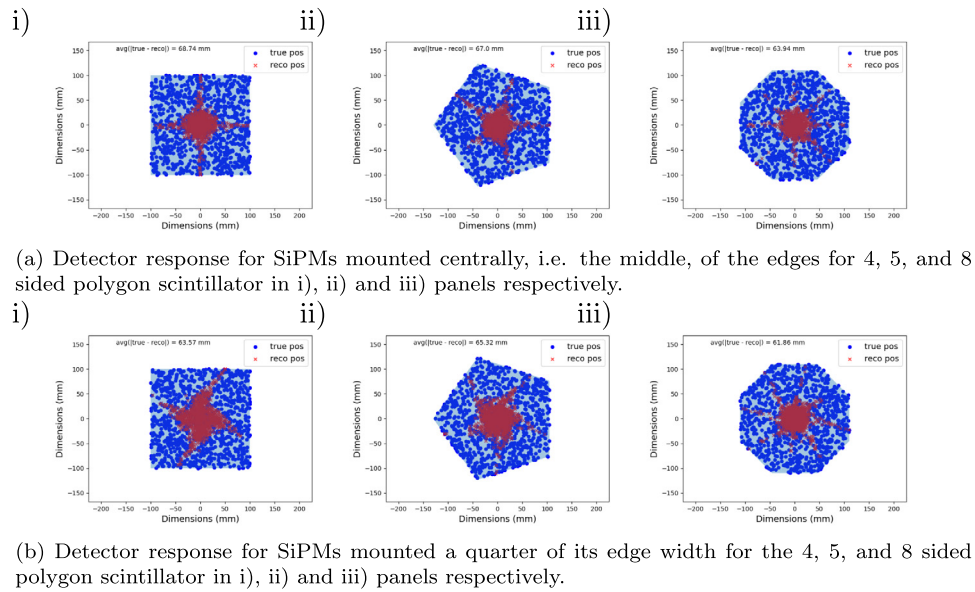
**Fig. 8.** Cumulative reconstructed (red marks) and true (blue dots) positions for the analytical reconstruction method based on the weighted average approach. Different detector geometries are considered, where one SiPM photosensor is located in the middle of each detector side in Fig. 8(a), or at a quarter of its edge width in Fig. 8(b). The average distance between the reconstructed and true position is also reported in each figure. (For interpretation of the references to colour in this figure legend, the reader is referred to the web version of this article.)



(a) True events centred on $(x, y) = (-62.5, 12.5)$    (b) True events centred on $(x, y) = (-12.5, 12.5)$

(c) True events centred on $(x, y) = (12.5, 62.5)$    (d) True events centred on $(x, y) = (87.5, 87.5)$
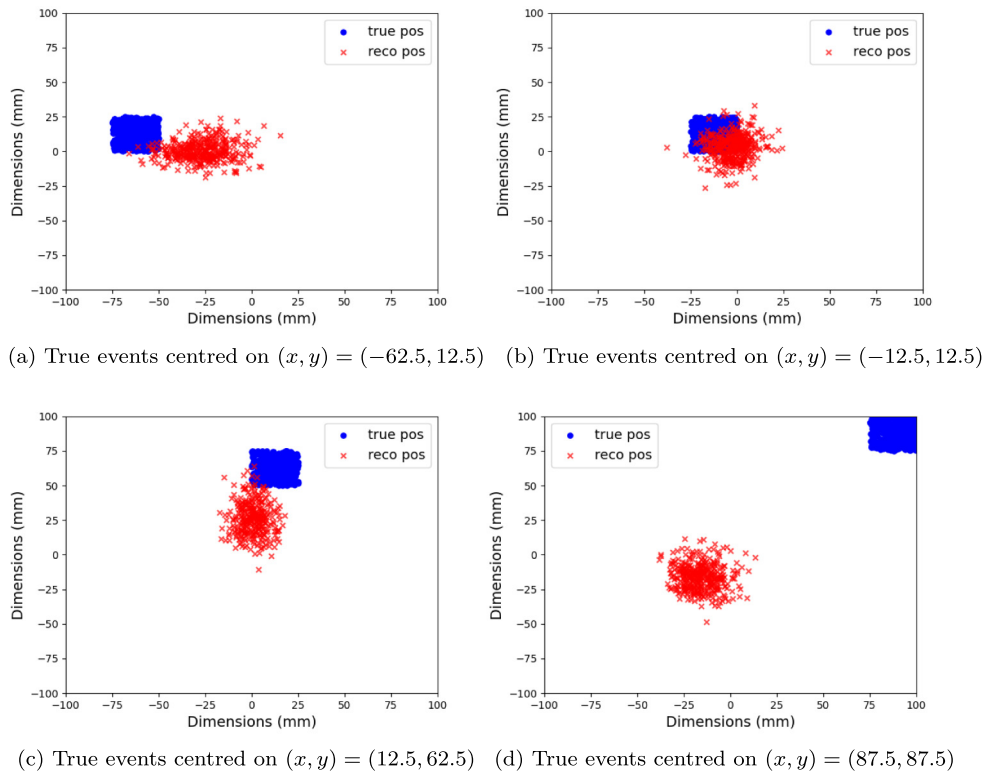
**Fig. 9.** True (blue dots) events within a 12.5 mm region, and resulting reconstructed (red marks) positions using the weighted average analytical method on a square geometry where one SiPM photosensor is located in the middle of each the detector side. Dimensions are shown in [mm]. Subsamples of true muon locations are displayed exclusively in each plot. (For interpretation of the references to colour in this figure legend, the reader is referred to the web version of this article.)

approximately $6 \times 10^5$ for the training set, $1 \times 10^5$ for the validation set and the remaining $1 \times 10^5$ for the testing set).

The data consists of a true position coordinate where the muon was incident on the scintillator and several intensity measurements from the various SiPMs that are optically linked to the scintillator. In the training data we have true positions that distributed over a fixed grid, this emulates how training data with known positions might realistically

be available. For example, one might measure real muon positions by placing a small scintillator on top of the main scintillator which could, in a binary manner, detect if a muon passed through both or not. By placing this small trigger-scintillator at several points along a grid on the main scintillator surface and recording events only when the two scintillators coincide, we will be able to record the final scintillator intensities while also knowing the muon incidence positions. These

(a) True events centred on $(x, y) = (-62.5, 12.5)$  (b) True events centred on $(-12.5, 12.5)$

(c) True events centred on $(x, y) = (12.5, 62.5)$  (d) True events centred on $(x, y) = (87.5, 87.5)$
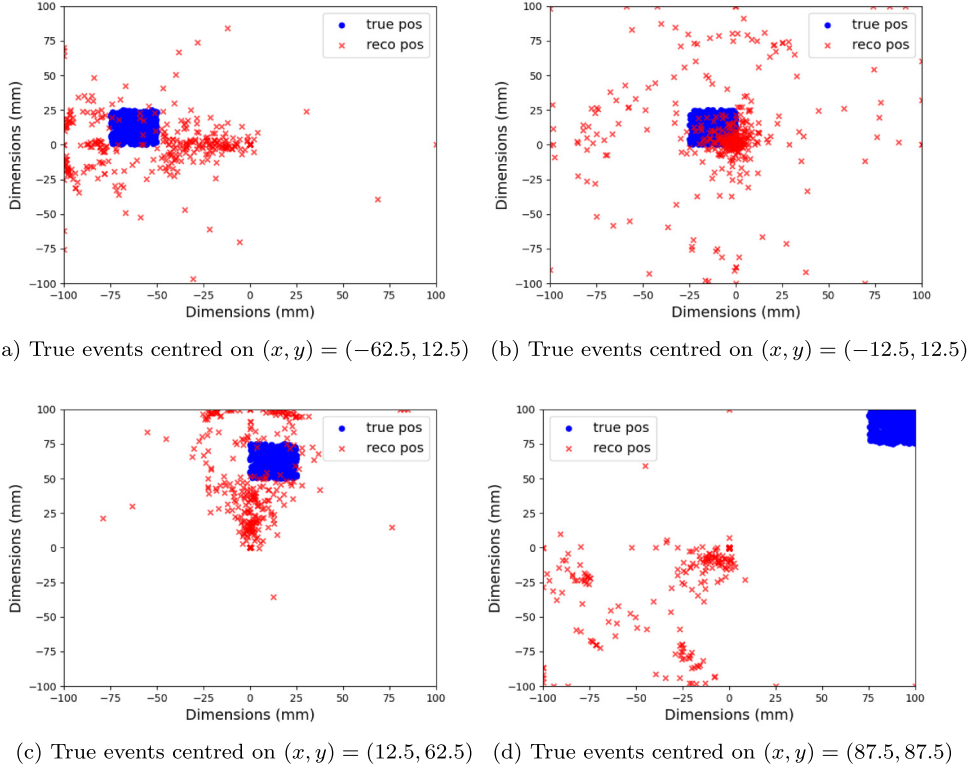
**Fig. 10.** Similar to Fig. 9 but now showing example reconstruction estimates for the analytic method, with subsamples of initial muon event locations centred in a region of 12.5 mm in blue dots and the resulting estimate in red cross, for the $200 \times 200$ mm$^2$ square detector. This analytical model made use of a method of position [20] given by Eq. (2), where the light absorption coefficient $\alpha$ is fixed to its nominal value [15] and the noise term $\tau$ is negligible with respect to the $I_0$ factor. (For interpretation of the references to colour in this figure legend, the reader is referred to the web version of this article.)

positions will however be limited to positions on that the grid we choose with a given resolution dependent on that small scintillator size. As a result, although we do not generate such a configuration in practice, we can provide insight to the performance of AI within such a realistic limitation in this work.

For our simulated data the grid we used was 39 by 39 resulting in 1521 total grid locations. We used an equal amount of training events from each of these grid positions in the training. In contrast, the testing data has continuous position coordinates, as an unknown muon could enter anywhere on the scintillator. This limitation recreates the data that would be available in practise and leads to the algorithm performances worsening by 7–15 percent over the ideal case. For every variation in geometry and photosensor position/number the machine learning algorithm shown was retrained.

### 5.1. Probabilistic Neural Network

Modified Probabilistic Neural Networks (PNN) have previously been attempted in the context of indoor positioning systems [23]. We implement a similar model here for our event location on the scintillator surface. This was implemented without using a standard PNN package to allow the flexibility to perform modifications.

Each event produces an intensity reading at one of the photosensors, forming a vector of intensities $\vec{I}$ for that event. The collection of intensity vectors for all events that share the same grid position $\vec{x}_k$ is given by $\mathbf{I}_{\vec{x}_k}$.

For a given testing event $\vec{I}_{test}$, the distances in intensity space are calculated for each training point $\vec{I}_i \in \mathbf{I}_{\vec{x}_k}$ that has its true position at $\vec{x}_k$. This is used to calculate a score $S_k$ for the particular position $\vec{x}_k$, where a hyper-parameter $\sigma_k$ is introduced that quantifies a length scale for each grid position on the scintillator.

$$S_k = \sum_{I_i \in \mathbf{I}_{\vec{x}_k}} exp\left(-\frac{|\vec{I}_{test} - \vec{I}_i|}{2\sigma_k}\right). \tag{3}$$

The probability that $\vec{I}_{test}$ was located at position $\vec{x}_k$ may then be calculated as

$$P(\vec{x}_k | \vec{I}_{test}) = \frac{S_k}{\sum_j S_j}, \tag{4}$$

and the predicted position is given by the probability-weighted average for all positions

$$\vec{x}_{pred} = \sum_i P(\vec{x}_i | \vec{I}_{test}) \vec{x}_i. \tag{5}$$

An advantage of this method is the ability to adjust the $\sigma$ parameter at each given point. This is particularly useful as certain areas of the scintillator will have varying uncertainty in their reconstruction accuracy. Both the analytical and machine learning methods implemented often struggle to reconstruct points along the edges of the scintillator, leading to poor performance in these areas. By optimising values of $\sigma$ for points along the edges, it is possible to change their probability weightings and increase the reconstruction performance.

While this method allows a unique $\sigma_k$ to be optimised for each grid point that our training events cover, it is not computationally feasible to optimise for this many hyperparameters in our case. Therefore the $\sigma$ hyperparameters were assigned by splitting the scintillator into three distinct regions. A centre region for points within 30 mm of the centre were all assigned $\sigma_{centre}$. A middle layer for points between 30 mm and 60 mm from the centre were all assigned $\sigma_{middle}$. All points further than 60 mm were assigned $\sigma_{outer}$. In Fig. 11 we explore the reconstruction recovery performance for several example $\sigma$ values, from the most central concentrated in Fig. 11(a), to a more dispersed distribution in Fig. 11(b) and finally the least centrally concentrated $\sigma$ values in Fig. 11(c). The respective values of $\sigma_{centre}$, $\sigma_{middle}$ and $\sigma_{outer}$ were found using a grid search over various combinations and selecting the parameters based on the reconstruction performance when applied to the validation set.

**Table 4**

Machine learning algorithm performance comparison, using the error radius (the 1 $\sigma$ confidence interval of all separation distances) and the average, mean, of the separation distance between the known 'true' muon event and the machine learning predicted location for a $200 \times 200$ mm$^2$ square scintillator with SiPMs in the edges/corners (given by Fig. 3(c) and light yield recovery pattern in the leftmost example of Fig. 6(c)).

| Algorithm | Error radius [mm] | Average distance [mm] |
|---|---|---|
| Probabilistic Neural Networks | 31.4 | 26.71 |
| Multilayer Perceptron Network | 37.68 | 32.28 |
| XGBoost Algorithm | 30.29 | 26.35 |

**Table 5**

Radial $1\sigma$ confidence intervals (in mm) for various square scintillation edge width sizes and number of SiPM photosensors employed, with the four initial SiPMs in the edge corners (as given by Fig. 3(c); light yield pattern of Fig. 4)a. Subsequent pairs of photosensors placed in the middle of opposing sides, resulting in the recovery pattern seen in Fig. 12.

| Scintillator edge width | Separation distance error [mm] | | |
|---|---|---|---|
| [mm] | 4 SiPMs | 6 SiPMs | 8 SiPMs |
| 100 | 13.35 | 10.44 | 7.80 |
| 150 | 20.59 | 16.66 | 12.91 |
| 200 | 29.01 | 23.15 | 17.95 |

This simple set-up increases performance over using a single $\sigma$ value for all points. However, this segmentation introduces a component to the algorithm construction that may result in less comparable results when tested on different scintillator geometries.

### 5.2. Multilayer Perceptron Neural Network

A standard Multilayer Perceptron Neural Network was implemented in Tensorflow [24]. This network accepts $n$ intensities as an input, and produces two outputs: the $x$ and $y$ coordinates of the event.

Different network architectures were assessed using the validation dataset results. The best performing architecture was a 6 hidden layer network, with 16 neurons per layer all using the Rectified Linear Unit (ReLu) activation function. Dropout was implemented on all hidden layers with probability of 0.2. The final layer consisted of two outputs with linear activation functions, these were the $x$ and $y$ coordinates.

### 5.3. XGBoost

Gradient boosting is a machine learning technique that provides predictions using an ensemble of decision trees. One popular implementation is the XGBoost Python package [25] which we have used for our data. The number of trees and the maximum depth of each tree were varied as hyperparameters and selected using *GridSearchCV*. For our data this consisted of 200 trees with a maximum depth of 6. We used the default values for eta (learning rate) 0.3 and gamma (min split loss) 0.

### 5.4. Comparison of techniques

The three algorithms and their resulting performance are compared in Table 4. The first comparison metric (middle column) is the error radius, the distance at which a 1 $\sigma$ confidence interval is attained for the separation between true and predicted event locations. The second metric is the mean separation distance between all actual positions and their respective predicted positions. The general trend is that the Multilayer Perceptron Network under-performs compared to the PNN or XGBoost which have similar respective results. As discussed previously, our implementation of PNN required some human decision in the segmentation that would not necessarily be replicable on different scintillator geometries. Combining this with the fact that XGBoost has a lower computational cost than the PNN method, we determine that XGBoost is a suitable solution to adopt for low-cost detectors in reality.

## 6. Detector design

The success of the machine learning approach to evaluating muon event positions relative to the analytic model gives us confidence to continue to explore the design of a muon detector in terms of number of photosensors and the scintillator geometry. We begin by systematically increasing the number of SiPMs around the square scintillator, with yellow pixels showing high light yield in Fig. 4 indicating the position of the photosensors. Different simulations were retrained with the XGBoost set-up mentioned previously in Section 5.3. We also relax

the previous constraint of training event true positions being confined to a fixed grid. We report the radial 1$\sigma$ confidence interval for each simulation in Table 5.

Using these overall results, the recovery of the radial 1$\sigma$ confidence $r_{\text{sep}}$ appears to follow a simple linear relationship with the size of the scintillator (L) and number of photosensors (N) given by

$$r_{\text{sep}} \approx 30.65 \text{ mm} \left( \frac{L}{200 \text{ mm}} \right) \left( \frac{4}{N} \right), \tag{6}$$

using simple linear regression (with fixed, zero, intercept) resulting in $R^2 = 0.99$. The optimal set-up for a given experiment may therefore in practice be decided by considering the required count rate (scaling as $L^2$), the intended accuracy of the reconstruction $r_{\text{sep}}$ and cost of each $N$ SiPM component.

The visualisation provided in Fig. 12 demonstrates that the algorithm struggles to identify points along the edges of the scintillator. This explains the success of the techniques that allow variable predictive parameters in different regions of the scintillator, such as the outlined probabilistic neural network method in Section 5.1. The computationally and time intensive tuning of these parameters however is a challenge for experimenting with them over many design iterations as in this work.

### 6.1. Circular design

It might be hoped that a circular geometry could alleviate the effect of 'dead zones' in the recovery accuracy along the edges seen in the square scintillator design in Section 3. However, the circular shaped detector does not only fail to resolve these issues but, perhaps surprisingly, significantly under-performs in the recovery when compared to a square detector of identical area.

In Fig. 13 we see the same structure as in Fig. 12 but with dramatically larger diagonal features (revealing quite clearly the position of the SiPM photosensors in each instance). Reflecting this, the recovery performance given by the 1-$\sigma$ distance error for the circular case as compared with the square geometry, given in Table 6, are correspondingly much larger.

### 6.2. Polygon designs

As part of the design of a low cost detector, we would hope to minimise the number of SiPMs used, and hence explore different polygon shapes and placement of the photosensors to determine if there is a performance increase possible. We implement the XGBoost algorithm for various detector polygon geometries (in terms of increasing edge count, from three to eight, i.e. triangle to octagon) explored when using either three or four SiPMs alone.

As is shown in Table 7, the effect of increasing number of edges for fixed number of SiPMs, i.e. four, is to increase the average recovery error (and a noticeable worsening when placed in the middle of an edge). Essentially, this result demonstrates that increasing edge counts is to asymptotically reach the case of the circular scintillator which offered the worst performance of all geometries. In Table 8, we explore this performance with only three SiPMs, ensuring that there

(a) Most centrally weighted $\sigma$ values

(b) Less centrally weighted $\sigma$ values

(c) Least centrally weighted $\sigma$ values
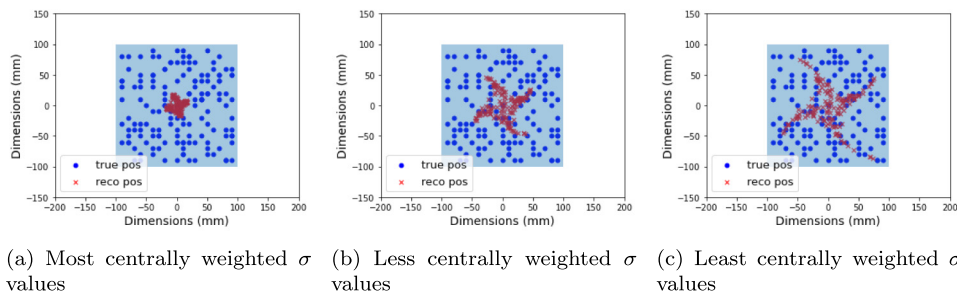
**Fig. 11.** The effect of changing the three $\sigma$ values ($\sigma_{centre}, \sigma_{middle}, \sigma_{outer}$) assigned to Eq. (3) for reconstructing positions. All images are for the same validation set. Blue points are the actual muon event positions used in Geant4. Red points are the algorithm's predicted muon positions. By adjusting the $\sigma$ values of the different areas the algorithm is better able to capture the true response of the scintillator. (For interpretation of the references to colour in this figure legend, the reader is referred to the web version of this article.)



(a) Square-shaped scintillator with four SiPMs in the corners as in configuration Fig. 4a)

(b) Square-shaped scintillator with six SiPMs in configuration Fig. 4b)

(c) Square-shaped scintillator with eight SiPMs in configuration Fig. 4c)
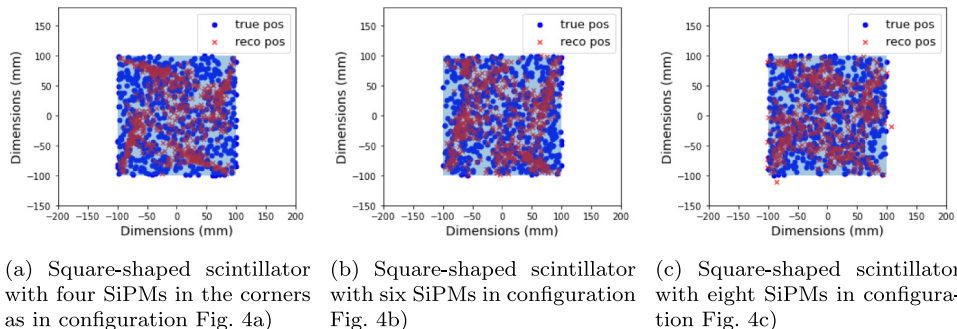
**Fig. 12.** The effect of increasing number of photosensors for the $200 \times 200$ mm$^2$ square scintillator. Blue points are the actual muon event positions used in Geant4. Red points are the algorithm's predicted muon positions. We note that the improvement in the position reconstruction average given in Table 6 is also seen visibly as an improvement in the general recovery spread (i.e. diminishing diagonal features). (For interpretation of the references to colour in this figure legend, the reader is referred to the web version of this article.)



(a) Circular-shaped scintillator with four SiPMs in the corners as in configuration Fig. 5a)

(b) Circular-shaped scintillator with six SiPMs in configuration Fig. 5b)

(c) Circular-shaped scintillator with eight SiPMs in configuration Fig. 5c)
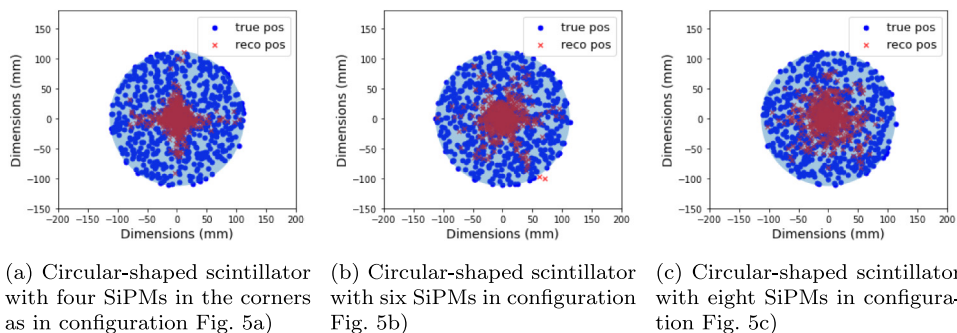
**Fig. 13.** As in Fig. 12 the effect of increasing number of photosensors in the performance of the XGBoost machine learning recovery accuracy, but now for the circular scintillator of radius 97.7 mm. Blue points are the actual muon event positions used in Geant4. Red points are the algorithm's predicted muon positions. (For interpretation of the references to colour in this figure legend, the reader is referred to the web version of this article.)

are different symmetries in the SiPM spacing's around a geometry of increasing numbers of edges. As might be expected the overall performance is poorer due to the one fewer SiPM photosensors, but the general trend of diminishing performance with increasing edges remain (as does the finding that positioning the photosensor in the middle of an edge is markedly worse). The performance for the final geometry, the octagon, is actually reasonably similar (albeit poor) if either three or four SiPMs were used. This can be seen as more an indication of the finite scintillator size and the event error approaching that magnitude rather than a convergence in performances in a positive sense.

From this we can conclude that symmetric sight-lines and/or multiple internal reflections result in diminished performance for the algorithm. Having more than one detector per edge (as given earlier in Table 5) is preferential for performance, but critically the resulting detector design should minimise the number of edges.

## 7. Discussion

In this work we explored, using Geant4 simulations, the feasibility and optimal design of a muon detector based around low-cost SiPM photosensors monitoring a plastic scintillator. The reconstruction of the muon event position with only four SiPM photosensors was a challenge for the analytic model, as explored in Section 4, which saw us then explore machine learning (ML) techniques.

In Section 5 we explored three standard ML-techniques in the literature, a Probabilistic Neural Network, a Perceptron Neural Network and a gradient boosted decision tree scheme (XGBoost [25]). As Table 4 indicates, the performance of the later was the best for recovery of muon event locations when using a four SiPM square scintillator and, due to both simplicity of methodology and computational performance, was selected to further explore detector designs.

As the intention was to optimise the design for future low-cost muon detectors we explored the number of the SiPM photosensors, the

**Table 6**

Radial $1\sigma$ confidence intervals for estimated event reconstruction in $200 \times 200$ mm² square detectors with SiPMs placed in the edges/corner, then increasing numbers placed in pairs in the middle of opposing sides of the square, see indicative light yield from yellow pixels in Fig. 4. This is compared to the 195 mm diameter circular detector geometries (of equivalent area) with increasing number of SiPM photosensors evenly distributed around the circumference, see yellow pixel for indicative distribution in Fig. 5. The square always outperforms the circular design, compare the recovery distributions of Figs. 12 and 13 to see this by eye. Moreover, the initial edge position for the square also provides superior reconstruction to either the middle or quarter cases explored in Tables 7 and 8.

| SiPM count | Square [mm] | Circle [mm] |
|---|---|---|
| 4 | 29.01 | 82.94 |
| 6 | 23.15 | 81.01 |
| 8 | 17.95 | 71.30 |

**Table 7**

Average distance ($1\sigma$ confidence interval) in [mm] between the predicted and actual position for four SiPMs. Photosensors were positioned either a quarter along an edge or in the middle of an edge for the middle and last columns respectively. Middle positions are indicated by Fig. 3(a) (light yield from Fig. 6(a)) and Quarter positions in Fig. 3(b) (light yield from Fig. 6(b)).

| Edges | Quarter [mm] | Middle [mm] |
|---|---|---|
| 4 | 33.7 (41.35) | 56.1 (72.99) |
| 5 | 37.1 (42.99) | 56.6 (72.81) |
| 6 | 45.1 (55.26) | 59.9 (75.73) |
| 7 | 51.3 (62.48) | 59.9 (74.86) |
| 8 | 56.3 (70.97) | 64.6 (83.9) |

**Table 8**

As with Table 7 the average distance ($1\sigma$ confidence interval) in [mm] between the predicted and actual position but now for only three SiPMs. Photosensors were positioned either a quarter along an edge or in the middle of an edge for the middle and last columns respectively. Middle positions are indicated by Fig. 6(a) and Quarter positions in Fig. 6(b).

| Edges | Quarter [mm] | Middle [mm] |
|---|---|---|
| 3 | 40.1 (46.53) | 65.5 (80.59) |
| 4 | 42.4 (50.86) | 61.8 (79.89) |
| 5 | 48.3 (58.52) | 61.5 (80.38) |
| 6 | 55.7 (69.33) | 63.4 (79.82) |
| 7 | 57.6 (72.48) | 65.1 (81.07) |
| 8 | 60.1 (75.65) | 68.3 (88.55) |

geometry of the detector and the placement of the SiPMs. In Section 6 we showed the improvement of the event reconstruction accuracy with increasing number of photosensors for the square scintillator (as well as the size of the scintillator) given in Table 5. This resulted in a simple linear relationship between positional accuracy and the average distance between the photosensors around the square detector, shown in (6).

In an effort to lower the costs of constructing such a detector in reality, we explored whether detector geometries for *fixed SiPM photosensors counts* could help in the reconstruction. The four SiPM photosensors deployed in various locations along polygons from squares to octagons in Table 7 showed a systematic reduction in performance. This finding was confirmed for three photosensors in the triangle to octagon case in Table 8. Furthermore, the placement of the SiPMs matter too; the middle or quarter spacing along an edge (as given by Fig. 6(a) and Fig. 6(b) respectively) is always inferior to placing at the edge/corner.

These findings all suggest that the optimal design of a low-cost muon detector is also surprisingly simple: cover in reflective coating a plastic scintillator of square geometry, place SiPMs at the edges/corners (to increase positional accuracy use additional SiPMs placed in opposite pairs in the middle of the scintillator edges) and use the XGBoost machine learning algorithm for event reconstruction. Of course, it is also entirely possible that real-world scintillators have sufficiently complex internal structures that the linear relationship between positional accuracy and the number of SiPMs employed will break down in practice.

This design is by no means the best, or only one, imaginable but our theoretical exploration suggest it should be competitive. Improvements to such a design can include the exploration of the thickness of the scintillator slabs, as well as exploring more advanced machine learning techniques. Indeed, the next steps can also include the challenge of designing a low-cost muon detector that can recover the true trajectory of passing muons. Fully integrating trajectory recovery across multiple detector layers, essentially recovering a joint fit, to measure the angle of incidence of muons for a square design is non-trivial. In particular, we would need to modify the simulation process to inject muons over the full angular range with varying energies, in a distribution [12]. It might also be anticipated that training a machine learning algorithm for the entire problem-case of trajectory recovery over multiple layers (as opposed to training on individual slabs) could offer improved recovery accuracy. This will be explored in future work.

## 8. Conclusion

In this study, we explored the factors that might influence the design of a low-cost muon detector, based around plastic scintillators and simple SiPMs photosensors. This worked utilised Geant4 simulations to model a muon radiation field incident on scintillators of varying size and geometry, and track the expected light yield at key locations around the edge where various numbers of SiPMs can be affixed. The theoretical intensity values recorded were then used to determine the predicted muon event location using both analytic and machine learning algorithms. As shown in Section 4, the former struggled to recreate the known event locations while for the latter, several techniques were explored and ultimately XGBoost [25] was found to perform best.

Using the boosted gradient method we then attempted to derive a relationship between the reconstruction accuracy for a given detector size and SiPM photosensor count, resulting in a linear increase in the reconstruction positional error with increasing edge width of a square detector and decreasing with number of photosensors evenly distributed around the perimeter of the scintillator, see Eq. (6).

The performance of the selected XGBoost scheme with differing detector geometries, and locations of the photosensors around those geometries, was explored in Sections 6.1 and 6.2. Perhaps surprisingly, the recovery of events for circular designs was incredibly poor. This may be seen as the asymptotic limit of increasing edges to the detector, going from square to octagon, which resulted in systematically diminishing performance for a fixed number of SiPMs. The location of the SiPMs themselves along the polygon edge was also an important driver of performance, with photosensors in the middle of a polygon edge leaving dead zones of low light yield recovery and hence poor reconstruction accuracy. Ultimately, placing four SiPMs in the edge corners of a square appeared to offer the best location of muons on the detector, this simple design is strongly recommended by the suite of Geant4 simulations explored in this work to guide future low-cost muon detectors.

## CRediT authorship contribution statement

**J. Heredge:** Methodology, Formal analysis, Software, Writing - original draft, Writing - review & editing. **J.W. Archer:** Investigation, Software, Data curation, Writing - original draft, Writing - review & editing. **A.R. Duffy:** Conceptualization, Methodology, Writing - review & editing, Supervision, Project administration, Funding acquisition. **J.M.C. Brown:** Resources, Writing - review & editing. **S. Guatelli:** Resources, Writing - review & editing, Supervision. **F. Scutti:** Methodology, Formal analysis, Software, Visualization, Writing - review & editing. **S. Krishnan:** Data curation, Investigation, Resources. **C. Webster:** Data curation, Resources.

**Declaration of competing interest**

The authors declare that they have no known competing financial interests or personal relationships that could have appeared to influence the work reported in this paper.

**Acknowledgements**

**References**

[1] G. Charpak, S. Majewski, F. Sauli, The scintillating drift chamber: A new tool for high-accuracy, very-high-rate particle localization, Nucl. Instrum. Methods 126 (3) (1975) 381–389.

[2] J. Szabelski, D.A. Iordache, P.E. Sterian, I. Tunaru, Charge coupled devices as particle detectors, Adv. High Energy Phys. 2013 (2013) 425746,

[3] P. Homola, D. Beznosko, G. Bhatta, Ł. Bibrzycki, M. Borczyńska, Ł. Bratek, et al., Cosmic-ray extremely distributed observatory, Symmetry 12 (11) (2020).

[4] C. Cattani, B. Mitrica, Design study of an underground detector for measurements of the differential muon flux, Adv. High Energy Phys. 2013 (2013) 641584, http://dx.doi.org/10.1155/2013/641584.

[5] C.H. Lee, J. Son, T.-H. Kim, Y.K. Kim, Characteristics of plastic scintillators fabricated by a polymerization reaction, Nucl. Eng. Technol. 49 (3) (2017) 592–597.

[6] P. Buzhan, B. Dolgoshein, L. Filatov, A. Ilyin, V. Kantzerov, V. Kaplin, et al., Silicon photomultiplier and its possible applications, Nucl. Instrum. Methods Phys. Res. A 504 (1–3) (2003) 48–52.

[7] V. Babiano, L. Caballero, D. Calvo, I. Ladarescu, P. Olleros, C. Domingo-Pardo, $\gamma$-Ray position reconstruction in large monolithic LaCl3(Ce) crystals with SiPM readout, Nucl. Instrum. Methods Phys. Res. A 931 (2019) 1–22.

[8] L. Wu, C.-H. Chen, Q. Zhang, A mobile positioning method based on deep learning techniques, Electronics 8 (1) (2019) 59.

[9] S. Agostinelli, J. Allison, K.a. Amako, J. Apostolakis, H. Araujo, P. Arce, et al., GEANT4—a simulation toolkit, Nucl. Instrum. Methods Phys. Res. 506 (3) (2003) 250–303.

[10] J. Allison, K. Amako, J. Apostolakis, H. Araujo, P. Arce, M. Asai, et al., Geant4 developments and applications, IEEE Trans. Nucl. Sci. 53 (2006) 270–278.

[11] J. Allison, K. Amako, J. Apostolakis, P. Arce, M. Asai, T. Aso, et al., Recent developments in Geant4, Nucl. Instrum. Methods Phys. Res. A 835 (2016) 186–225.

[12] P. Shukla, S. Sankrith, Energy and angular distributions of atmospheric muons at the earth, Internat. J. Modern Phys. A 33 (30) (2018) 1850175.

[13] P. Arce, D. Bolst, M.-C. Bordage, J.M.C. Brown, P. Cirrone, M.A. Cortés-Giraldo, D. Cutajar, G. Cuttone, L. Desorgher, P. Dondero, A. Dotti, B. Faddegon, C. Fedon, S. Guatelli, S. Incerti, V. Ivanchenko, D. Konstantinov, I. Kyriakou, G. Latyshev, A. Le, C. Mancini-Terracciano, M. Maire, A. Mantero, M. Novak, C. Omachi, L. Pandola, A. Perales, Y. Perrot, G. Petringa, J.M. Quesada, J. Ramos-Méndez, F. Romano, A.B. Rosenfeld, L.G. Sarmiento, D. Sakata, T. Sasaki, I. Sechopoulos, E.C. Simpson, T. Toshito, D.H. Wright, Report on G4-med, a geant4 benchmarking system for medical physics applications developed by the geant4 medical simulation benchmarking group, Med. Phys. 48 (1) (2021) 19–56, http://dx.doi.org/10.1002/mp.14226, http://arxiv.org/abs/https://aapm.onlinelibrary.wiley.com/doi/pdf/10.1002/mp.14226.

[14] V. Ivanchenko, A. Bagulya, S. Bakr, M. Bandieramonte, D. Bernard, M.-C. Bordage, et al., Progress of Geant4 electromagnetic physics developments and applications, in: EPJ Web of Conferences, Vol. 214, EDP Sciences, 2019, p. 02046.

[15] Eljen Technology, General purpose plastic scintillator EJ-200, EJ-204, EJ-208, EJ-212, 2016, https://eljentechnology.com/products/plastic-scintillators/ej-200-ej-204-ej-208-ej-212.

[16] R. Craun, D. Smith, Analysis of response data for several organic scintillators, Nucl. Instrum. Methods 80 (2) (1970) 239–244.

[17] Eljen Technology, Reflective paint EJ-510, EJ-520, 2018, https://eljentechnology.com/products/accessories/ej-510-ej-520.

[18] ON Semiconductor, C-series SiPM sensors, 2018, https://www.onsemi.com/products/sensors/silicon-photomultipliers-sipm/c-series-sipm.

[19] R. Pani, F. Vittorini, M. Cinti, P. Bennati, R. Pellegrini, S. Ridolfi, et al., Revisited position arithmetics for LaBr$_3$:Ce continuous crystals, Nuclear Phys. B Proc. Suppl. 197 (2009) 383–386.

[20] C. Lerche, J. Benlloch, F. Sánchez, N. Pavón, N. Gimnéz, M. Fernández, et al., Depth of interaction detection with enhanced position-sensitive proportional resistor network, Nucl. Instrum. Methods Phys. Res. A 537 (2005) 326–330.

[21] P. Virtanen, R. Gommers, T.E. Oliphant, M. Haberland, T. Reddy, D. Cournapeau, et al., Scipy 1.0: Fundamental algorithms for scientific computing in python, Nat. Meth. 17 (2020) 261–272.

[22] Z. Li, M. Wedrowski, P. Bruyndonckx, G. Vandersteen, Nonlinear least-squares modeling of 3D interaction position in a monolithic scintillator block, Phys. Med. Biol. 55 (21) (2010) 6515–6532.

[23] C. Chen, L. Yin, Y. Chen, R. Hwang, A modified probability neural network indoor positioning technique, in: 2012 International Conference on Information Security and Intelligent Control, 2012, pp. 317–320.

[24] M. Abadi, P. Barham, J. Chen, Z. Chen, A. Davis, J. Dean, et al., TensorFlow: A system for large-scale machine learning, in: 12th USENIX Symposium on Operating Systems Design and Implementation (OSDI 16), 2016, pp. 265–283.

[25] T. Chen, C. Guestrin, Xgboost: A scalable tree boosting system, in: Proceedings of the 22nd ACM SIGKDD International Conference on Knowledge Discovery and Data Mining, in: KDD '16, Association for Computing Machinery, New York, NY, USA, 2016, pp. 785–794.